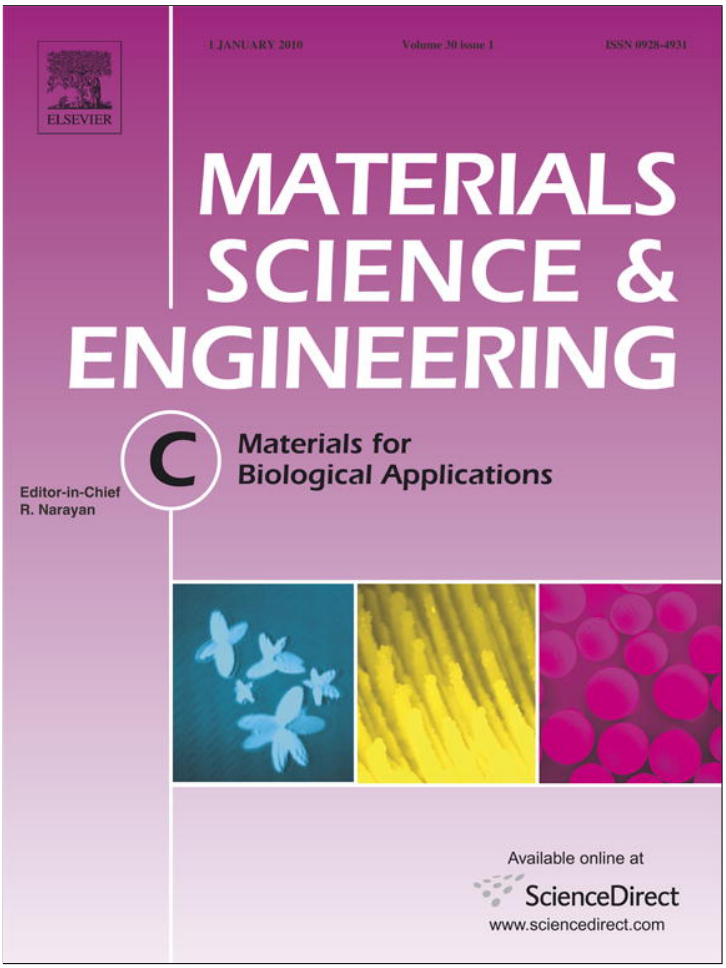

Materials Science and Engineering C 30 (2010) 62–70

Contents lists available at ScienceDirect

Materials Science and Engineering C

journal homepage: www.elsevier.com/locate/msec

Polyethylene ionomer-based nano-composite foams prepared by a batch process and MuCell® injection molding

Hidetomo Hayashi [a], Tomoki Mori [a], Masami Okamoto [a,*], Satoshi Yamasaki [b], Hiroshi Hayami [b]

[a] Advanced Polymeric Nanostructured Materials Engineering, Graduate School of Engineering, Toyota Technological Institute, Hisakata 2-12-1, Tempaku, Nagoya 468-8511, Japan
[b] Polymer Materials Technology R&D Department Electronics & Materials R&D Laboratories, Sumitomo Electric Industries, Ltd., Shimaya, Konohana-ku, 1-1-3, Osaka, 554-0024, Japan

ARTICLE INFO

Article history:
Received 4 August 2009
Accepted 26 August 2009
Available online 4 September 2009

Keywords:
Ionomer
Neutralization
Nano-composites
MuCell® technology

ABSTRACT

To understand the correlation between foamability and melt rheology of polyethylene-based ionomers having different degrees of the neutralization and corresponding nano-composites, we have conducted the foam processing via a batch process in an autoclave and microcellular foam injection molding (FIM) process using the MuCell® technology. We have discussed the obtainable morphological properties in both foaming processes. All cellular structures were investigated by using field emission scanning electron microscopy. The competitive phenomenon between the cell nucleation and the cell growth including the coalescence of cell was discussed in light of the interfacial energy and the relaxation rate as revealed by the modified classical nucleation theory and rheological measurement, respectively. The FIM process led to the opposite behavior in the cell growth and coalescence of cell as compared with that of the batch process, where the ionic cross-linked structure has significant contribution to retard the cell growth and coalescence of cell. The mechanical properties of the structural foams obtained by FIM process were discussed.

1. Introduction

Over the last few years, the utility of inorganic nanoscale particles as filler to enhance the polymer performance has been established. Of particular interest is a recently developed nano-composite technology consisting of a polymer and organically modified layered filler (organo-clay) because they often exhibit remarkably improved mechanical and various other material properties as compared with those of virgin polymer or conventional composite (micro/macro-composites) [1–5]. These concurrent property improvements are well beyond what can be generally achieved through the micro/macro-composites' preparation.

The effect of organo-clay on the crystal structure [6,7] (including polymorphism) and foam processing [8–12] of the matrix semi-crystalline polymer has been investigated in nano-composites. In our recent publications, we have reported on the foam processing of polypropylene (PP)/organo-clay [13], poly(L-lactide) (PLA)/organo-clay [8] and polycarbonate (PC)/ organo-clay [14] in a batch process by using supercritical carbon dioxide (CO_2) as a physical foaming agent.

They described the morphological correlation between the dispersed organo-clay particles with nanometer dimensions in the bulk and the formed closed- and/or open-cellular structure after foaming [8]. The incorporation with nano-clay induced heterogeneous nucleation because of a lower activation energy barrier compared with homogeneous nucleation as revealed by the characterization of the interfacial tension between bubble and matrix. The grown cells having a diameter of ~200 nm were localized along the dispersed nano-clay particles in the cell wall. The dispersed nano-clay particles acted as nucleating sites for cell formation and the cell growth occurred on the surfaces of the clays. The nano-composites provided excellent polymeric foams having high cell density ($\geq 10^{13}$ cells/cm^3) at low temperature with high CO_2 pressure condition.

On the other hand, microcellular foam injection molding (FIM) [15] have been largely applied to produce structural foams that consist of two compact polymer skin layers enclosing a foamed core, it must be described as inhomogeneous materials with varying properties across the part thickness [16]. The microcellular FIM is characterized by cell densities on the order of 10^9 cells/cm^3 or more and cell sizes on the order of 10 μm or less.

In both foaming processes (batch and FIM), the evolution of foam morphologies depends on the processing parameters like melt temperature and gas content, whereas lower (melt) temperatures and higher gas contents induce a finer cell size distribution [17], which can be discussed as consistent for all polymeric foams. The bubble growth itself is controlled by the gas diffusion from the matrix polymer into the cells, the melt viscosity of the material and overall pressure drop [18]. To study the above-mentioned effects on the obtainable morphological and mechanical properties of the nano-composite foams, it is necessary to select different nano-composites having a wide range of melt viscosity. Accordingly, either nucleation effects or rheological effects should induce the intended differences in morphology.

* Corresponding author.
E-mail address: okamoto@toyota-ti.ac.jp (M. Okamoto).

0928-4931/$ – see front matter © 2009 Elsevier B.V. All rights reserved.
doi:10.1016/j.msec.2009.08.009

Table 1
Composition and characteristic parameter of ionomers and nano-composites.

Samples	ZnO / phr	Neutralization[a] / %	Organo-clay / wt.%
Ionomer 0/55	0	55	0
Ionomer 3/89[b]	3	89	0
Ionomer/clay 20/0/58	0	58	20
Ionomer/clay 20/3/78	3	78	20
Ionomer/clay 20/6/97	6	97	20

[a] The value measured by titrimetric analysis.
[b] The sample is prepared using quarternized ammonium salt.

Table 2
Injection molding parameters for solid samples.

	Ionomer 0/55	Ionomer 3/89	Ionomer/clay 20/0/58	Ionomer/clay 20/3/78
Nozzle temperature / °C	215	215	215	215
Mold temperature / °C	40	40	40	40
Injection speed / mm / s	68.6	14.8	64.8	53.2
Pack/hold pressure /MPa	150	150	200	220
Injection time /s	1.0	4.7	1.1	1.3
Cooling time /s	30.0	30.0	30.0	30.0

In this study, we have attempted to investigate the correlation between foamability and melt rheology of polyethylene-based ionomers having different degrees of the neutralization and corresponding nano-composites via a batch process in an autoclave. The ionic cross-linked structure in the ionomer expects significant contribution to retard the cell growth and coalescence of a cell, especially in an ionomer having a higher degree of neutralization. For nano-composite foaming, experimentally, nano-clay particles will lead to an increase in cell density after foaming. The FIM process using the MuCell® technology is also adopted to generate structural foams. Such a comparison between batch and FIM will be worthwhile not only for assessing the foam morphology but also for studying the foaming performance in nano-composite for MuCell® technology.

2. Experimental section

2.1. Materials

An ionomer resin (Himilan 1706: MA content = 15 wt.%, Zinc oxide (ZnO) content = 3.70 wt.%, neutralization = ~55% and melt flow index (MI) = 4.1 g/10 min) purchased from Du Pont-Mitsui Polychemicals Co., LTD., was used as a polymer matrix. An organo-clay used in this study was supplied by Southern Clay Products, Inc., and was synthesized by replacing Na^+ ions in montmorillonite (MMT) (cation exchange capacity (*CEC*) of 90 mEq/100 g, thickness ≈ 1 nm, average length of 150–200 nm) with di-octadecyl di-methylammonium ($DC_{18}DM$) cation by ion exchange.

2.2. Nano-composites preparation

For nano-composites preparation, the organo-clay (powder) and ionomer (pellets) were first dry-mixed by shaking them in a bag. The mixture was then melt extruded using a twin-screw extruder (PCM-30, Ikegai Corp.) operated at 200 °C (screw speed = 100 rpm, feed rate = 120 g/min) to yield nano-composite strands. The strands were palletized and dried under vacuum at 60 °C for 48 h to remove water. The nano-composite prepared with 20 wt.% of organo-clay was denoted as ionomer/clay 20/0/58. The abbreviations of various ionomers and the corresponding nano-composites prepared using zinc oxide (ZnO) (as a neutralizating agent) also are presented in Table 1. For the nano-composites including ZnO, the degree of neutralization exhibits large increment due to the presence of organo-MMT. Presumably, the dispersed organo-clay acts as catalytic sites for the neutralization [19]. For ionomer 3/89, the degree of neutralization is controlled by using ZnO (3 phr) and dodecyl tri-methyl ammonium chloride (as a neutralizating catalyst) [19].

2.3. Foam processing

The foam processing was conducted on ionomers and corresponding nano-composites in an autoclave (TSC-WC-0096, Taiatsu Techno Co) by using supercritical CO_2 [4]. Basically, the physical foam processing (batch process) used in this study consists of three stages: (1) CO_2 saturation in the sample at desired temperature; (2) cell nucleation when the release of CO_2 pressure started (supersaturated CO_2) and cell growth to an equilibrium size during the release of CO_2; and (3) cell stabilization *via* cooling process of the foamed system. In the first stage, the specimen ($10 \times 20 \times 0.9$ mm^3 = width × length × thickness) was inserted into an autoclave (96 mL) and CO_2 pressure was increased up to 30 MPa at various temperatures [8]. The temperature inside the autoclave was increased and maintained at a predetermined temperature using a cartridge heater for temperature control. In this study, we conducted the experiments at two different foaming temperatures (T_f) (90 and 100 °C), just above the melting temperature (~88 °C) of ionomer. The sample in the autoclave was heated from room temperature to T_f in 0.5 h to achieve the equilibrium state, and then dissolved in CO_2 for 5 h under the pressure range between 14 and 30 MPa. For such a long time of CO_2 dissolution into the sample, CO_2 has already been saturated in the sample at fixed T_f. In the second stage, the CO_2 pressure was rapidly reduced (within 3 s) in order to supersaturate the specimen with CO_2 gas [8]. The thermodynamic instability resulted in the formation of a large number of cell nuclei. After releasing the CO_2 pressure, the formed foams were stabilized *via* cooling by liquid-CO_2 at room temperature, and then removed carefully from the autoclave and kept at ambient temperature.

The injection molding machine (J85AD, The Japan Steel Works, Ltd.) has a 85 ton clamping force and is equipped with a MuCell® technology (Trexel Inc., MA, USA). Supercritical nitrogen gas (N_2) was

Table 3
Injection molding parameters for MuCell® samples (MC-1 and MC-2).

	Ionomer 0/55		Ionomer 3/89	Ionomer/clay 20/0/58		Ionomer/clay 20/3/78	
	MC-1[a]	MC-2[a]	MC-1	MC-1	MC-2	MC-1	MC-2
Nozzle temperature / °C	215		215	215		215	
Mold temperature / °C	40		40	40		40	
Injection speed / mm / s	51.1	56.1	93.0	25.0	25.0	20.8	17.1
Pack/hold pressure / MPa	15	20	150	40	120	100	170
SCF injection ratio[b] / wt.%	0.02		0.08	0.02		0.08	
SCF injection pressure / MPa	10.2	23.6	14.4	25.1	25.2	24.3	24.7
Injection time / s	0.9	1.1	0.9	2.0		2.7	3.2
Cooling time / s	90.0		60.0	90.0		90.0	

[a] The processing conditions of MC-1 and MC-2 are corresponding to a density reduction of 10 and 5%, respectively.
[b] Supercritical fluid (SCF) N_2 in wt.% is calculated from Eq. (1).

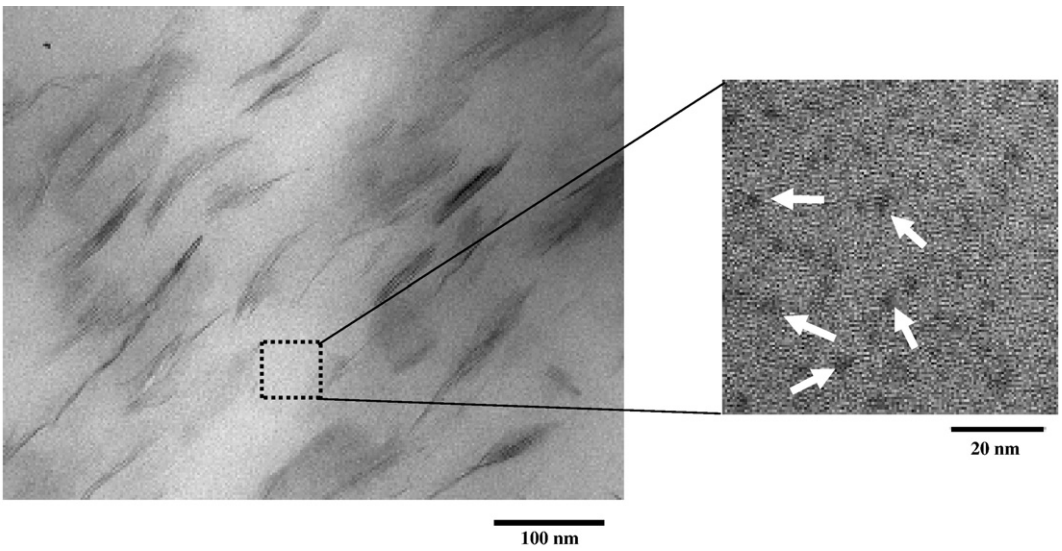

Fig. 1. Bright field TEM images of ionomer/clay 20/0/58. The dark entities are cross-section and/or face of intercalated-and-stacked nano-clay layers, and the bright areas the matrix. The enlarge parts shown are from the nano-sized ionic aggregates in the original images.

used as the physical blowing agent at loading of 0.08 and 0.2 wt.%, and was injected into the screw barrel according to the MuCell® procedure. The processing parameters are presented in Tables 2 and 3. The Supercritical fluid (SCF) N_2 in wt.% is defined following Eq. (1).

$$wt.\%\ SCF = \frac{27.8(\dot{m})t}{m} \tag{1}$$

where $\dot{m}$ is the mass flow rate of the SCF in kg/h, t is the SCF injection time (s), m is the shot weight in g, and 27.8 is a conversion factor. The processing conditions of MC-1 and MC-2 correspond to a density reduction of 10 and 5%, respectively. Using this method, the structural foamed tensile bars (ASTM D638-03) were injection molded.

The cell structures were investigated by using a field emission scanning electron microscope (FE-SEM) (S-4700, Hitachi Co.). The samples were freeze-fractured in liquid nitrogen and sputter-coated with platinum at an argon pressure of 0.1 Torr for 1.5 min at a current of 10 mA. The average cell radius (d) and the mean cell wall thickness (δ) were determined from the data of FE-SEM observation. The

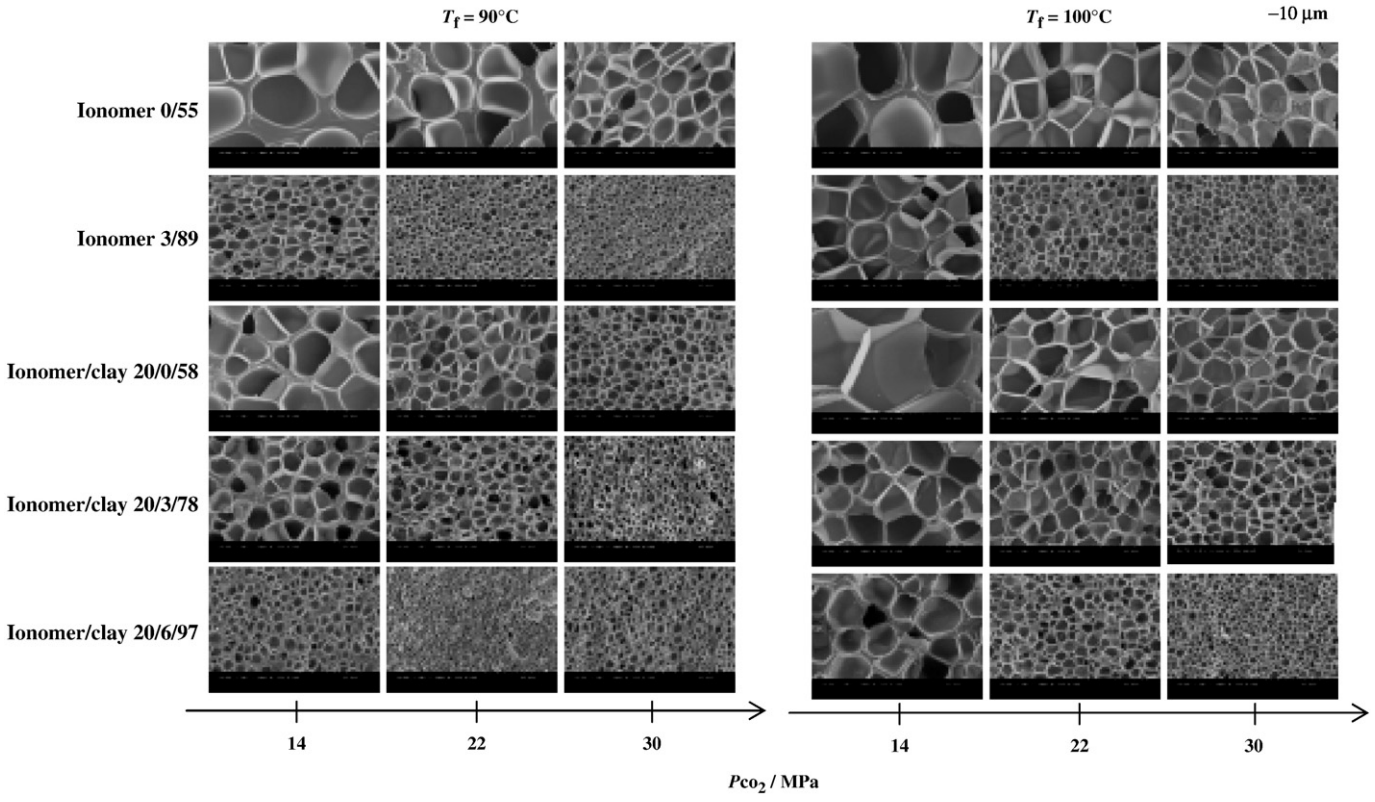

Fig. 2. Typical results of FE-SEM images of the fracture surfaces of the materials foamed at two different temperatures under the different isobaric saturation conditions (14, 22 and 30 MPa).

function for determining cell density (N_c) in cell/cm^3 is defined as Eq. (2) [14]:

$$N_c = \left[\frac{n}{A}\right]^{3/2} \quad (2)$$

where n is the number of cells in the area (A) of micrograph. The mass density of both pre-foamed (ρ_p) and post-foamed (ρ_f) in g/cm^3 samples were estimated by using the buoyancy method [8].

2.4. Characterization

2.4.1. Transmission electron microscopy (TEM)

Nanoscale structure of ionomer/clay 20/0/58 was investigated by means of TEM (H-7100, Hitachi Co.), operating at an accelerating voltage of 100 kV. The ultra thin sections (the edge of the sample sheet perpendicular to the compression mold) with a thickness of 80 nm were microtomed at −80 °C using a Reichert Ultra cut cryo-ultramicrotome without staining. The number of ionic aggregated domains, consisting of Zn^{2+}, in the micrograph was determined by the software.

2.4.2. Melt rheology

Melt rheological measurements were conducted on a RDAII instrument with a torque transducer capable of measurements in the range of 0.2–200 g cm. Dynamic oscillatory shear measurements were performed by applying a time dependent strain of $\gamma(t) = \gamma_o \sin(\omega t)$ and the resultant shear stress is $\sigma(t) = \gamma_o [G' \sin(\omega t) + G'' \cos(\omega t)]$, with G' and G'' being the storage and loss modulus, respectively. Measurements were conducted by using a set of 25 mm diameter parallel plates with a sample thickness of ~1.0 mm and in the temperature range of 100–180 °C. The strain amplitude was fixed to 10% to obtain reasonable signal intensities even at elevated temperature or low frequency (ω) to avoid the nonlinear response. For each sample investigated, the limits of linear viscoelasticity were determined by performing strain sweeps at a series of fixed ω's. The master curves were generated using the principle of time–temperature superposition and shifted to a common reference temperature (T_r) of 100 °C, which was chosen as the most representative of a typical processing temperature of ionomer.

2.4.3. Dynamic mechanical analysis (DMA)

Dynamic mechanical properties of both pre-foamed and post-foamed samples ($12 \times 35 \times 4$ mm^3 = width × length × thickness) were measured using a Reometrics Dynamic Analyzer (RDAII) in the tension–torsion mode. The temperature dependence of dynamic storage modulus (G') and tanδ of the samples were measured at a constant frequency (ω) of 6.28 rad/s, a strain amplitude of 0.05%, and in the temperature range of −150 to 150 °C with a heating rate of 2 °C/min. The thermal expansion coefficient (α) in mm/mm°C is calculated by Eq. (3):

$$\alpha = \frac{\Delta L}{\Delta T}\frac{1}{L_0} \quad (3)$$

where ΔL is the change in length in mm, ΔT is the change in temperature and L_0 is the original length of the sample (=35 mm). The value of α is selected in the temperature range of −150 to 0 °C because the existence of the thermally unstable crystals such as the poor chain packing or disordered crystals are observed above 0 °C [20].

3. Results and discussion

3.1. Ionomer-based nano-composite structure

Fig. 1 shows the results of TEM bright field images of ionomer/clay 20/0/58, in which dark entities are the cross-section of layered MMT nano-fillers. The figure shows the dispersion of the MMT within the ionomer matrix, and after a close look, permitting the observation of discrete nano-layers. The disorder and delaminated silicate layer structure with the thickness of ~16 nm is observed in each TEM

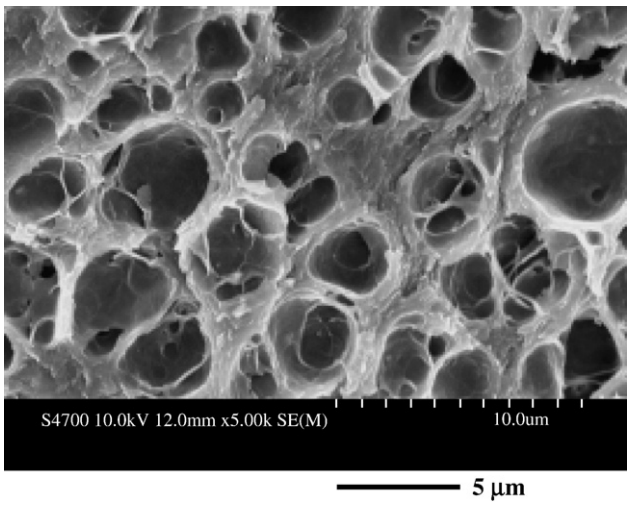

Fig. 3. FE-SEM image of the fracture surfaces of ionomer/clay 20/6/97 foamed at 90 °C under 30 MPa.

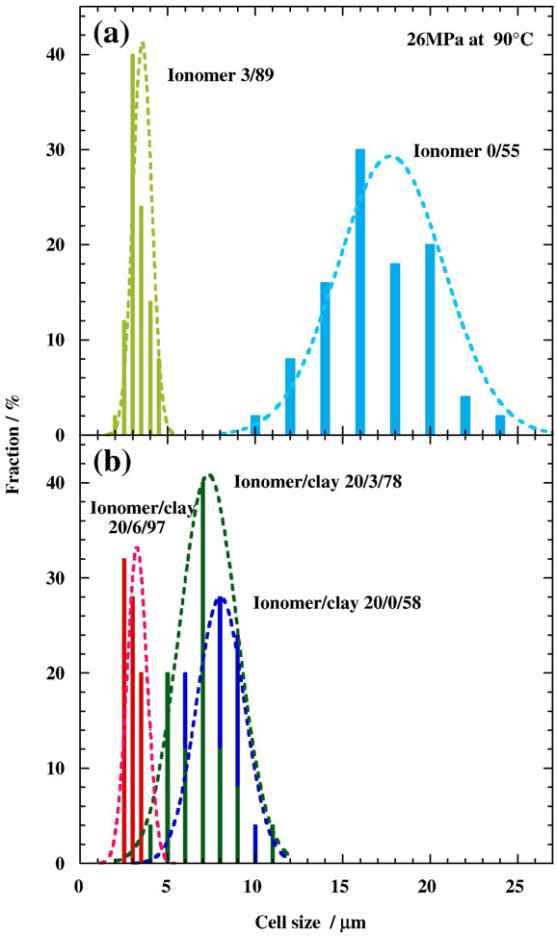

Fig. 4. Typical example for cell size distribution of foamed (a) ionomers and (b) nano-composites in experiment at 90 °C under 26 MPa. Average values 2d in μm and standard deviation σ_d in μm in the Gaussian fit through the data are 17.7 and 3.0 for ionomer 0/55, 3.5 and 0.5 for ionomer 3/89, 8.0 and 1.4 for ionomer/clay 20/0/58, 7.3 and 1.7 for ionomer/clay 20/3/78 and 3.3 and 0.6 for ionomer/clay 20/6/97 foams, respectively.

image. From the TEM it becomes clear that there are some intercalated-and-stacked silicate layers co-existing with the disordered or exfoliated MMT layers in the nano-composite structure. Only the stacked intercalated silicate layers are responsible for very sharp wide-angle X-ray diffraction (WAXD) reflection, whereas the disordered or exfoliated silicate layers have no periodic stacking and thus remain WAXD silent. The appearance of new peaks observed at diffraction angle $2\Theta \cong 2.91°$ (≅3.03 nm), 5.55° (≅1.59 nm) for ionomer/clay 20/0/58, were confirmed and these reflection were due to the (001) and (002) plane of MMT-DC_{18}DM (data not shown). Actually, there is a large anisotropy of the stacked silicate layers. The size of some of the stacked-silicate layers appears to reach about 100–150 nm in length and the interlayer distance as revealed by TEM observation is about 3 nm. This value is virtually the same as compared to WAXD data. Typically the large-in lateral size-MMT layers create stacked intercalated structure and the number of the stacked individual MMT layers is 5–7 for ionomer/clay 20/0/58, whereas the smaller layers tend to exfoliate [21]. A significant difference in the TEM images among the degree of neutralization is not observed.

In Fig. 1, the dark areas represent the nano-sized ionic aggregates similar to what is observed for other ionomers [22]. After a higher magnification, shown in the enlarged views, we clearly observe spheres with a domain size of approximately 2–3 nm (indicated with arrows). The ionic aggregates are randomly arranged in the ionomer matrix. The number of the aggregates (N_{ion}) can be estimated from the enlarged images. The calculated value of N_{ion} was 0.08–0.12 nm^{-2} for ionomer/clay 20/0/58 and 0.98–0.15 nm^{-2} for ionomer/clay 20/6/97. This result suggests that the ionic cross-linked density in the system of 20/6/97 is higher than that of matrix in the absence of ZnO (6 phr).

3.2. Morphology of foams via batch process

Fig. 2 shows the typical results of FE-SEM images of the fracture surfaces of the materials foamed at two different temperatures under the different isobaric saturation conditions (14, 22 and 30 MPa). All foams exhibit the closed-cell structure, which has a smaller cell size (d) and larger cell density (N_c) with increasing saturation pressure condition. A high CO_2 pressure (~30 MPa) provides a large supply of CO_2 molecules, which can subsequently form a large population of cell nuclei upon depressurization. At the same time, we consider here the effect of the pressure drop rate on the cell nucleation. An increase in pressure drop rate leads to the appearance of a large number of nucleated cells as compared with the slower pressure drop (~14 MPa). The incorporation of nano-clay shows smaller cell size and larger cell density compared with neat ionomer 0/55 foams. For ionomer/clay 20/6/97, the nano-composite foam exhibits the heterogeneous bimodal cell distribution as seen in Fig. 3. Experimentally, nano-clay particles lead to an increase in N_c. However, we cannot identify how the dispersed nano-clay particles act as nucleating sites for cell formation. This feature will be discussed later.

For all foams, we have calculated the distribution function of cell size from the FE-SEM images and the results are presented in Fig. 4. All foams nicely obeyed the Gaussian distribution. In the case of ionomer 3/89 foamed at 90 °C under high pressure of 26 MPa, we can see that the width of the distribution peak, which indicates the cell size distribution, becomes more narrow accompanied by the large degree

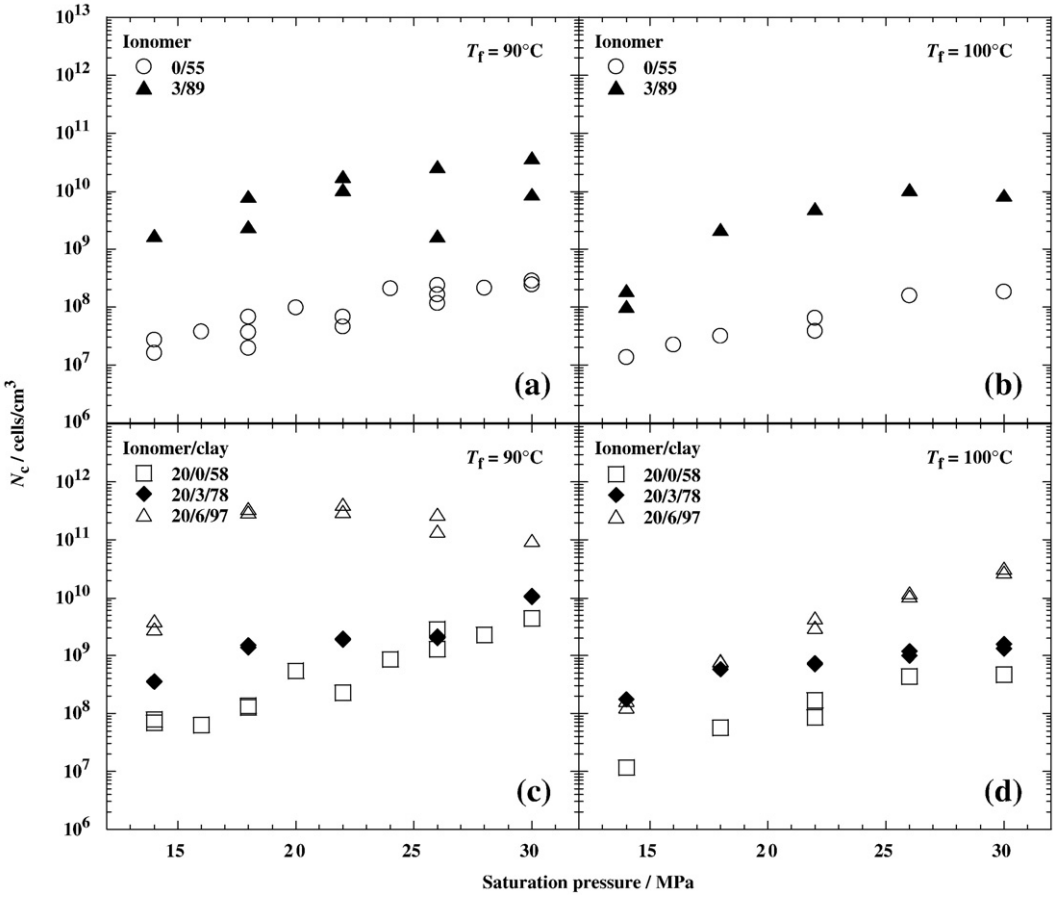

Fig. 5. CO_2 pressure dependence of the cell density (N_c) for ionomers ((a) and (b)) and nano-composites ((c) and (d)) foamed at two different T_fs (90 and 100 °C).

of neutralization (89%). This indicates that the melt viscosity and modulus in ionomer 3/89 have some contribution to retard the cell growth and coalescence of cell during foaming. The degree of the neutralization is mainly responsible for the cell formation as compared to the incorporation of nano-clay.

The dependence of the cell density at two different T_fs under different CO_2 saturation pressures is shown in Fig. 5. Throughout the whole pressure ranges, the cell density shows gradual increase with increasing CO_2 pressure, except in the case of ionomer/clay 20/6/97 at $T_f = 90$ °C. With decreasing saturation pressure condition (~14 MPa), all systems exhibit small cell density due to the low supply of CO_2 molecules, which can subsequently form a small population of cell nuclei upon depressurization [8].

In Fig. 6, we show the relations between $2d$ and N_c, in this study. The relations nicely obey in $2d \sim N_c^{-1/3}$. The ionomer/clay 20/6/97 foams enhance the value of N_c accompanied with the small value of $2d$ as compared with that of other nano-composite foams. The controlled structure is from $2d \cong 1$–$20\,\mu m$ with $N_c \cong 10^8$–10^{11} cells cm^{-3}. The deviation occurs beyond the value of $N_c \sim 10^{11}$ cell cm^{-3}. The downward deviation indicates that the heterogeneous bimodal cell distribution under the low foaming temperature (~90 °C) as seen in Fig. 3.

3.3. Characterization of interfacial tension

Both homogeneous and heterogeneous nucleation mechanisms may appear to be of comparable significance. All systems demonstrate that N_c increases systematically with an increase in CO_2 pressure up to 30 MPa. The cell nucleation in the heterogeneous nucleation system such as nano-composite foams may take place in the boundary between the matrix and the dispersed nano-clay particles. To clearly investigate the influence of internal surfaces of the dispersed nano-clay we characterized the interfacial tension between bubble and matrix by using modified classical nucleation theory [23]. According to the theory proposed by Suh and Colton, the rate of nucleation of cells per unit volume ($\dot{N}$) can be written as:

$$\dot{N} \sim Cf \exp\left[\frac{-\Delta G}{k_B T}\right] \tag{4}$$

where C is the concentration of CO_2 and/or the concentration of heterogeneous nucleation sites, f is the collision frequency of CO_2, ΔG is the activation energy barrier, k_B is the Boltzmann constant and T denotes absolute temperature. Moreover, the activation energy barrier is given by:

$$\Delta G = \frac{16\pi\gamma^3 S(\theta)}{3(\Delta P_{CO2})^2} \tag{5}$$

where γ is the interfacial tension between bubble and matrix, ΔP_{CO2} is the magnitude of the pressure quench during depressurization and $S(\theta)$ is the energy reduction factor for the heterogeneous nucleation (i.e., ionomer/clay).

The theoretical cell density is given by:

$$N_{\text{the or}} = \int_0^t \dot{N} dt \tag{6}$$

where t is the foaming time that takes approximately 3 s.

Generally we can observe the cumulative number of cell and apparent pressure quench depth. For this reason, our characterization of the interfacial tension is obtained from a rough approximation. We consider here the effect of the pressure drop rate on the cell nucleation. An increase in pressure drop rate leads to the appearance of a large number of nucleated cells as compared with the slower pressure drop (~14 MPa). For slower pressure drops the cell diameter but not the number of first formed cell increases. At the same time, under the increasing saturation condition (~30 MPa) we have to take the effect of the residue of CO_2 on the viscosity of the materials into consideration. For this reason the situation is very complex to explain well. This discussion is beyond the objective of this paper, and we will report separately. Assuming no effect of the coalescence of cell on the value of N_c, we estimate the interfacial energy ($\gamma S(\theta)^{1/3}$) of the systems calculated using Eqs. (4)–(6), i.e., the slope of the plots (N_c versus $1/\Delta P_{CO2}^2$). For all cases examined the plots conform to the straight lines (see Fig. 7) as predicted by Eqs. (4)–(6). The characteristic parameters of three systems are also summarized in Table 4. The evaluated result gives almost the same value (~6 mJ/m^2) and does not depend on the processing temperature and systems. The estimated values are in good agreement with that of other polymer–CO_2 system (~10 mJ/m^2) [8,24]. However, the nano-composite (ionomer/clay 20/0/58) foams exhibit smaller cell size and larger cell density without the significant difference in $\gamma S(\theta)^{1/3}$ as compared with neat ionomer 0/55 foams, suggesting that the dispersed silicate particles do not act as nucleating sites for cell formation. This trend reflects the relative importance of the cell growth and the coalescence of cell. That is, we have to take the viscosity effect (relaxation time) on the cell growth and coalescence of cell into consideration.

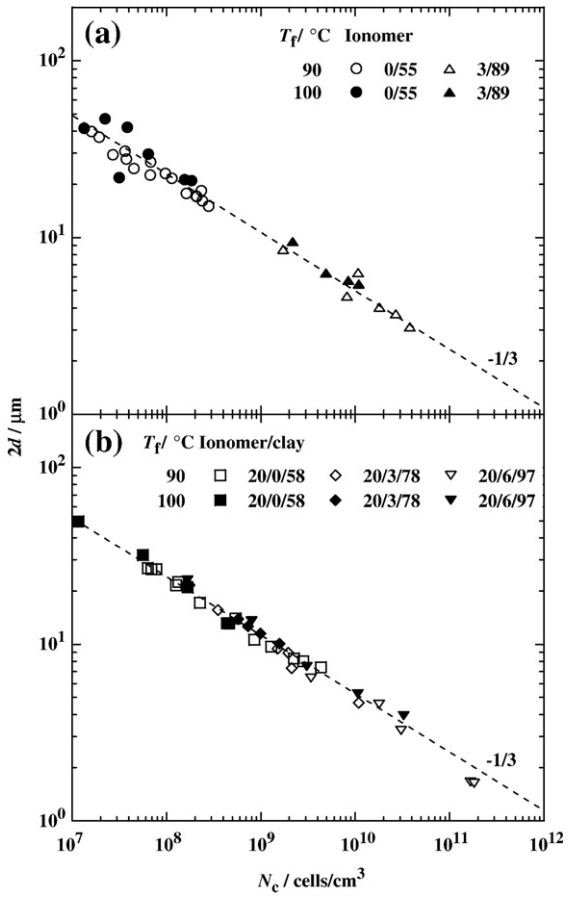

Fig. 6. Relation between cell size versus cell density for (a) ionomer and (b) nano-composite foams. The dashed line indicates the slope −1/3.

3.4. Melt rheology and relaxation time

To confirm the viscosity effect on the cell coalescence we investigated the flow behavior of the ionomers and the corresponding nano-composite. The slope of $G'(\omega)$ and $G''(\omega)$ versus the $a_T\omega$ is much smaller than 2 and 1, respectively. Values of 2 and 1 are expected for linear mono-dispersed polymer melts, and a large

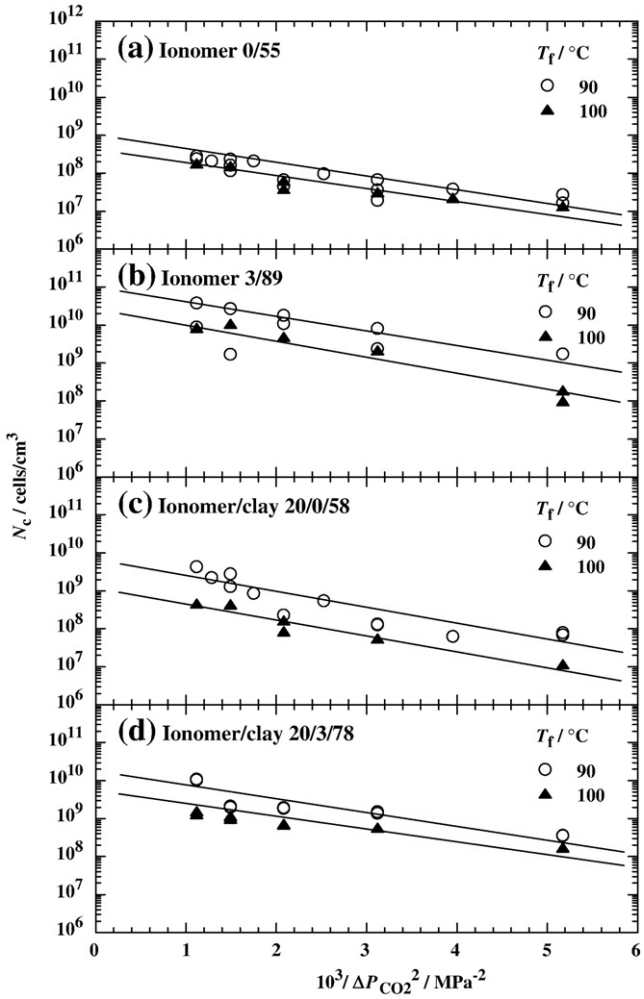

Fig. 7. Plots of cell density (N_c) versus reciprocal CO_2 pressure $1/(P_{CO2})^2$ for (a) ionomer 0/55, (b) ionomer 3/89, (c) ionomer/clay 20/0/58 and (d) ionomer/clay 20/3/78 foamed at two different T_f.

deviation may be due to the formation of the ionic cross-linked network structure in the melt state [19]. The temperature dependence frequency shift factor (a_T, Arrhenius-type) is used to generate master curves. The details of the rheological features were described in our previous paper [20]. To understand the generic dynamic rheology, the cross over frequency ω_{rel} in the master curve of the dynamic frequency sweep enables one to predict a relaxation time ($=1/\omega_{rel}$), which is determined from the measured master curve when tan δ is unity. Fig. 8 shows the results of the temperature dependence of relaxation rate (ω_{rel}), assuming that the rate is of Arrhenius-type.

Table 4
Characteristic interfacial parameter of systems at different T_f.

Systems	T_f / °C	$\gamma S(\theta)^{1/3}$ / mJ/m^2
Ionomer 0/55	90	5.2
	100	5.7
Ionomer 3/89	90	6.1
	100	6.7
Ionomer/clay 20/0/58	90	6.5
	100	6.5
Ionomer/clay 20/3/78	90	5.9
	100	5.3
Ionomer/clay 20/6/97	90	6.7
	100	6.7

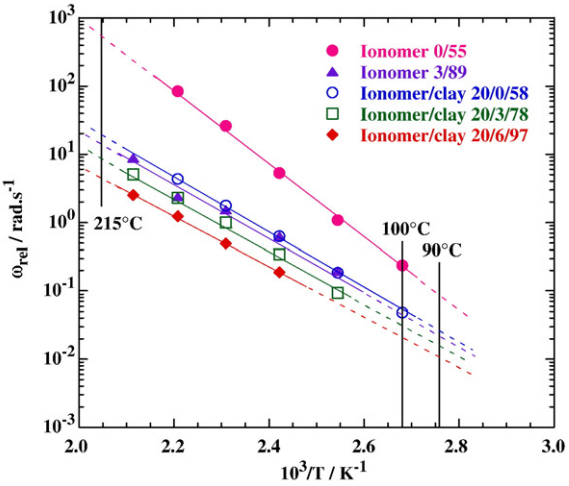

Fig. 8. Temperature dependence of characteristic relaxation rates (ω_{rel}) of ionomers and nano-composites. The foaming temperature ranges (90 and 100 °C for batch process, and 215 °C for FIM process) are shown.

For ionomer 3/89, the estimated relaxation rates are about 0.082–12.5 s^{-1} in the range of temperature between 100 and 180 °C. These values are much smaller than those of ionomer 0/55 (those are in fact 0.24–84.5 s^{-1}), suggesting that the ionic cross-linked density (the degree of the neutralization) is a dominant factor for the relaxation time scale. The slope that reflects the activation energy of each process exhibits a different value. The activation energy of the relaxation process is also estimated (see Table 5). An interesting feature is that in the range of temperature between 90 (batch process) and 215 °C (FIM process) this trend remains by extrapolation based on plotting ω_{rel} versus reciprocal temperature, $1/T$.

The ionic cross-linked structure has a significant contribution to retard the cell growth and coalescence of cell. For this reason, ionomer 3/89 foams lead to a large value of N_c accompanied with the small value of $2d$ as compared with that of ionomer 0/55 foams. That is, in the ionomer foaming the cell growth and coalescence of cell are dominant factor rather than the promoting heterogeneous nucleation. Meanwhile, for ionomer/clay 20/0/58, a same feature is observed as well as ionomer 3/89 foaming, implying that the nucleating effect of the dispersed nano-clay particles is overwhelmed (i.e., no enhancement of the nucleation).

3.5. Morphology of foams via FIM process

Fig. 9 shows the typical results of FE-SEM images of the fracture surfaces of the structural foams processed at two different conditions under FIM process (see Table 3). All structural foams consist of two compact polymer skin layers enclosing a foamed core. As well as the upper side as at the bottom side the layer thickness (skin layer thickness %) is measured at four points and averaged. However, in the case of MC-2 condition for nano-composites (ionomer/clay 20/0/58

Table 5
Activation energy of each system.

Systems	E_a / kJ/mol
Ionomer 0/55	104.9
Ionomer 3/89	92.2
Ionomer/clay 20/0/58	79.2
Ionomer/clay 20/3/78	76.7
Ionomer/clay 20/6/97	70.9

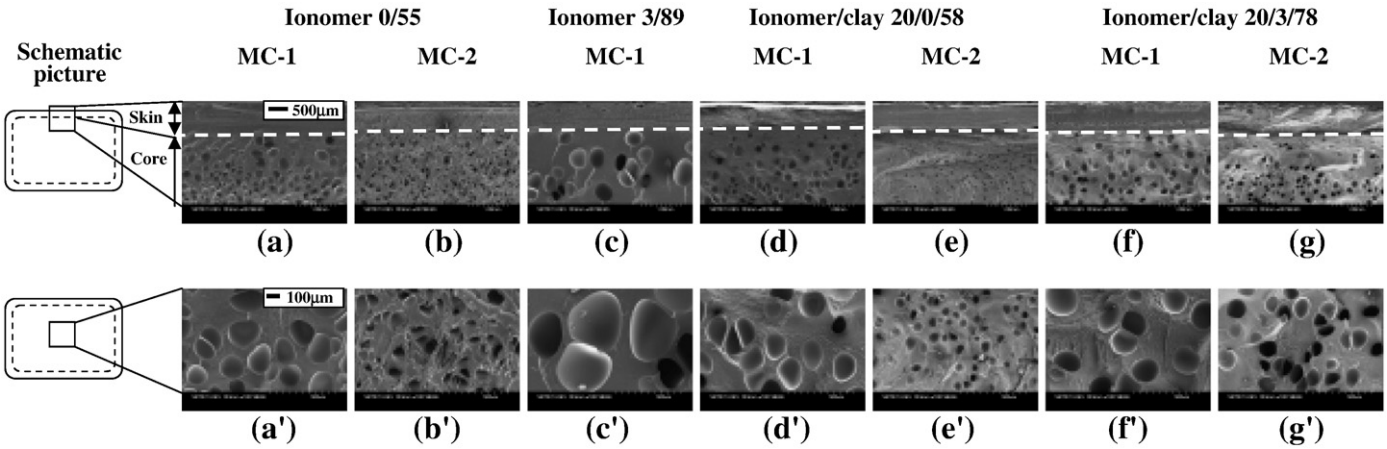

Fig. 9. Typical results of FE-SEM images of the fracture surfaces of the structural foams processed at two different conditions under FIM process. (a)–(g) skin layers enclosing the foamed core and (a′)–(g′) center area of the foamed core.

and ionomer/clay 20/3/78) the second layer is observed at the end of the skin layer to the center area of the foamed core (see Fig. 10). The cell size in this area exhibits much smaller (~10–30 μm) than that of the foamed core. The characteristic features of the obtained foams are presented in Fig. 11.

We noted here that, in the case of MC-1 (density reduction of 10%), all foams exhibit larger cell size and smaller cell density as compared with those of MC-2 condition (density reduction of 5%) except ionomer 3/89. This indicates that the different processing conditions have a rather pronounced effect of the morphology of the structural foams. The coalescence effect in the cellular core is a dominant factor rather than the promoting nucleation due to the low viscosity of the materials with a SCF N_2 of 0.2 wt.% at 215 °C.

For this reason, the FIM process in this study leads to bigger cell size and smaller cell density as compared with that of the batch process. The development of solidified skin layer can be explained easily by heat transfer. However, the skin layer thickness has no significant difference between these processing sets including injection molding of their solid (see Table 2).

Interestingly, the FIM process leads to the opposite behavior in the cell growth and coalescence of cell as compared with that of the batch process, where the ionic cross-linked structure has a significant contribution to retard the cell growth and coalescence of cell. At this moment, we are not able to propose the real mechanism of the cell formation in the FIM process. This will be clarified shortly.

3.6. Mechanical properties

The specific dynamic storage modulus (G') at −50 °C and the specific thermal expansion coefficient (α) in the temperature range of −150 to 0 °C of solids and foamed materials obtained by FIM process are summarized in Fig. 12. In the case of solid, there is a significant increase in G' and decreasing in α for all nano-composites as compared with that of ionomers. After structural foaming prepared by MC-1 condition, all nano-composite foams exhibit much higher enhancement in G' (200% for ionomer/clay 20/0/58, 210% for ionomer/clay 20/3/78) than those of the structural foam of the corresponding ionomers. This is due to the mechanistic reinforcement by the dispersed nano-clay particles in the cell wall [25]. The dispersed nano-clay particles seem to act as a secondary cloth layer to protect the cells from being deformed by external forces. At the same time, the reduction of the thermal expansion coefficient in the

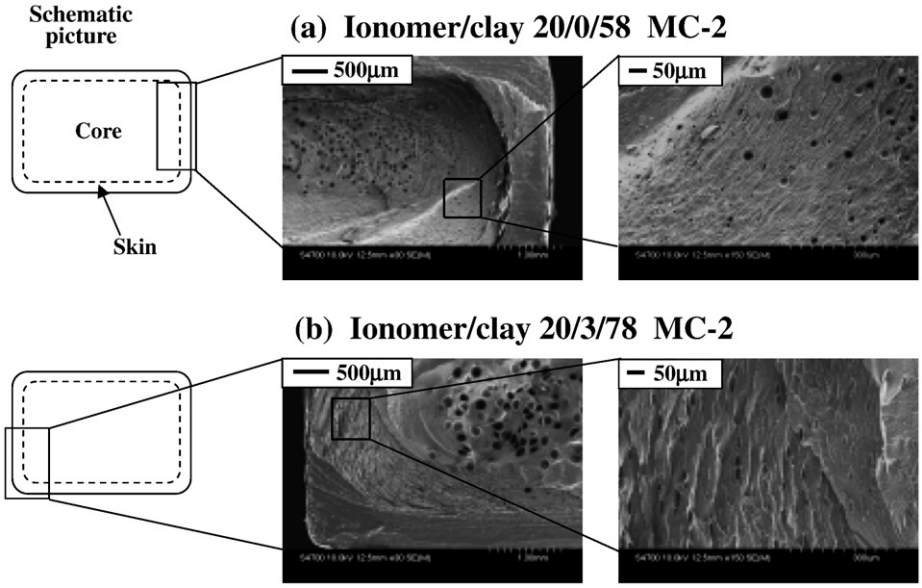

Fig. 10. Typical results of FE-SEM images of the fracture surfaces of the structural foams of (a) ionomer/clay 20/0/58 and (b) ionomer/clay 20/3/78 under MC-2 processing condition. The images shown are the second layer at the end of the skin layer to the center area of the foamed core.

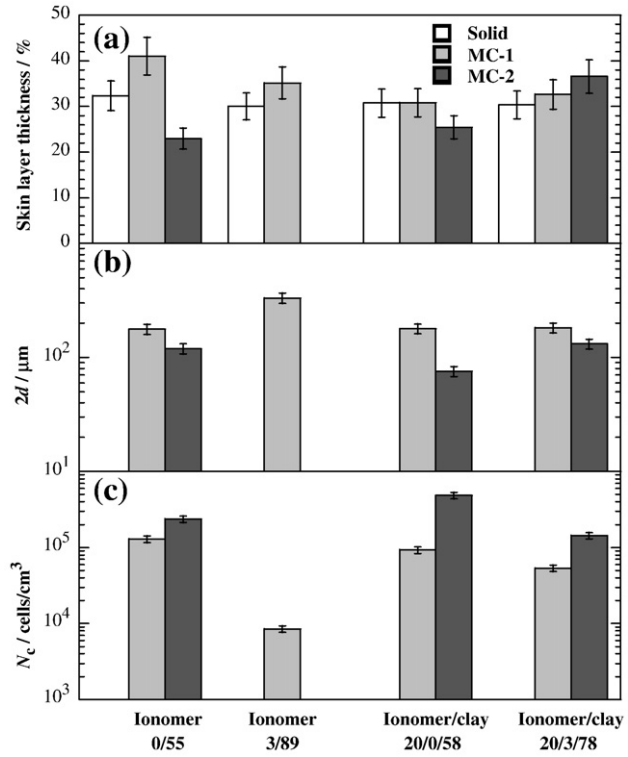

Fig. 11. Skin layer thickness, cell size ($2d$) and cell density (N_c) of the obtained structural foams. The values of the skin layer thickness in solid samples are shown for comparison.

nano-composite foams seems to stem from the mechanical constraint by the dispersed nano-clay particles [26]. For this reason, all nano-composite foams show significant reduction of α value and the value decreases up to 66% for ionomer/clay 20/0/58 and 53% for ionomer/clay 20/3/78 with MC-1 condition as compared with their structural foam of the ionomers. Unfortunately, in this study, no samples perpendicular to the mold-filing direction have been investigated. This issue will be discussed in more detail separately [27].

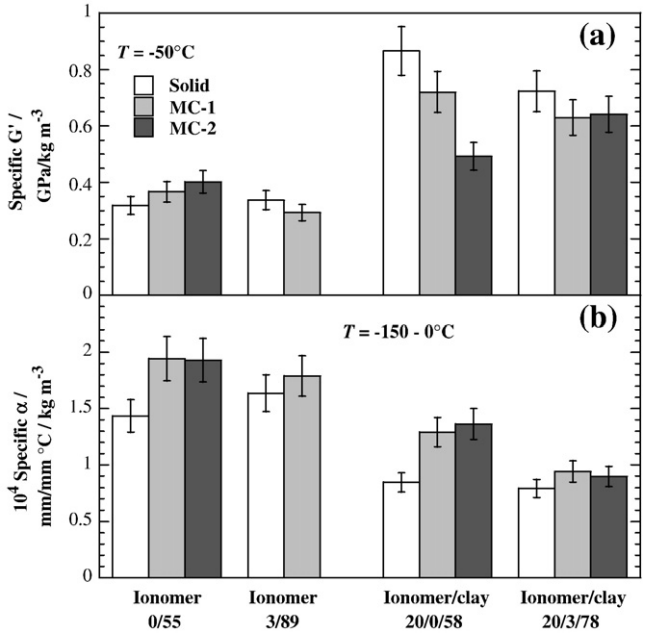

Fig. 12. (a) Specific dynamic storage modulus (G') at −50 °C and (b) specific thermal expansion coefficient (α) in the temperature range of −150 to 0 °C of solids and foams.

4. Conclusions

We have discussed the correlation between foamability and melt rheology of polyethylene-based ionomers having different degrees of the neutralization and corresponding nano-composites via a batch process in an autoclave and the FIM process using the MuCell® technology. In the batch process, the ionic cross-linked structure exhibited significant contribution to retard the cell growth and coalescence of cell. The degree of the neutralization is mainly responsible for the cell formation as compared to the incorporation of nano-clay particles. The ionomer/clay 20/6/97 foams enhanced the value of N_c accompanied with the small value of $2d$ as compared with that of other nano-composite foams. The controlled structure was from $2d \cong 1$–20 μm with $N_c \cong 10^8$–10^{11} cells cm^{-3}.

We have successfully prepared the structural foams processed at two different conditions under the FIM process. The coalescence effect in the cellular core is the dominant factor rather than the promoting nucleation due to the low viscosity of the materials with a SCF N_2 of 0.2 wt.% at high temperature (~215 °C). The FIM process led to bigger cell size and smaller cell density as compared with that of the batch process.

After structural foaming prepared by MC-1 condition, all nano-composite foam exhibit much higher enhancement in G' than those of the structural foam of the corresponding ionomers. At the same time, all nano-composite foams show significant reduction of α value and the value decreases up to 66% as compared with their structural foam of the ionomers.

Acknowledgments

This work was supported by the STAS Project (2005–2009) and the MEXT "Collaboration with Local Communities" Project (2005–2009).

References

[1] S. Sinha Ray, M. Okamoto, Prog. Polym. Sci. 28 (2003) 1539.
[2] R.A. Vaia, H.D. Wagner, Materials Today 7 (2004) 32.
[3] F. Gao, Materials Today 7 (2004) 50.
[4] A. Okada, A. Usuki, Macromol. Mater. Eng. 291 (2006) 1449.
[5] F. Hussain, M. Hojjati, M. Okamoto, R.E. Gorga, J. Compos. Mater. 40 (2006) 1511.
[6] K. Asia, M. Okamoto, K. Tashiro, Polymer 49 (2008) 4298.
[7] Y. Katoh, M. Okamoto, Polymer 50 (2009) 4718.
[8] Y. Ema, M. Ikeya, M. Okamoto, Polymer 47 (2006) 5350.
[9] L.J. Lee, C. Zeng, X. Cao, X. Han, J. Shen, G. Xu, Compos. Sci. Technol. 65 (2005) 2344.
[10] X. Cao, L.J. Lee, T. Widya, C. Macosko, Polymer 46 (2005) 775.
[11] A. Chandra, S. Gong, L.S. Turng, P. Gramann, H. Cordes, Polym. Eng. Sci. 45 (2005) 52.
[12] W. Strauss, N.A. D'Souza, J. Cell. Plast. 40 (2004) 229.
[13] P.H. Nam, M. Okamoto, P. Maiti, T. Kotaka, T. Nakayama, M. Takada, M. Ohshima, N. Hasegawa, A. Usuki, Polym. Eng. Sci. 42 (2002) 1907.
[14] Y. Ito, M. Yamashita, M. Okamoto, Macromol. Mater. Eng. 291 (2006) 773.
[15] H. Eckardt, K. Alex, Adv. In Plast. Tech. 1 (1981) 40.
[16] N. Mueller, G.W. Ehrenstein, J. Cell. Plast. 40 (2004) 45.
[17] C.B. Park, D.F. Baldwin, N.P. Suh, Polym. Eng. Sci. 35 (1995) 432.
[18] C.B. Park, N.P. Suh, Polym. Eng. Sci. 36 (1996) 34.
[19] T. Shigemori, M. Okamoto, S. Yamasaki, H. Hayami, Composites Part A: Appl. Sci. Manuf. 39 (2008) 1924.
[20] T. Mori, H. Hayashi, M. Okamoto, S. Yamasaki, H. Hayami, Composites Part A: Appl. Sci. Manu. 40 (2009) 1708–1716.
[21] S. Sinha Ray, K. Yamada, M. Okamoto, A. Ogami, K. Ueda, Chem. Mater. 15 (2003) 1456.
[22] J.A. Lefelar, R.A. Weiss, Macromolecules 17 (1984) 1145.
[23] J.S. Colton, N.P. Suh, Polym. Eng. Sci. 27 (1987) 485.
[24] S.K. Goel, E.J. Beckman, Polym. Eng. Sci. 34 (1994) 1137.
[25] M. Okamoto, P.H. Nam, M. Maiti, T. Kotaka, T. Nakayama, M. Takada, M. Ohshima, A. Usuki, N. Hasegawa, H. Okamoto, Nano Lett. 1 (2001) 503.
[26] P.H. Nam, M. Maiti, M. Okamoto, T. Kotaka, N. Hasegawa, A. Usuki, Polymer 42 (2001) 9633.
[27] H. Hayashi, M. Okamoto, S. Yamasaki, H. Hayami, in preparation.